ADVANCED FUNCTIONAL MATERIALS
www.afm-journal.de

Materials, Mechanics Designs, and Bioresorbable Multisensor Platforms for Pressure Monitoring in the Intracranial Space

Quansan Yang, Seungae Lee, Yeguang Xue, Ying Yan, Tzu-Li Liu, Seung-Kyun Kang, Yung Jong Lee, Seok Hwan Lee, Min-Ho Seo, Di Lu, Jahyun Koo, Matthew R. MacEwan, Rose T. Yin, Wilson Z. Ray, Yonggang Huang,* and John A. Rogers**

Pressures in the intracranial, intraocular, and intravascular spaces are important parameters in assessing patients with a range of conditions, of particular relevance to those recovering from injuries or from surgical procedures. Compared with conventional devices, sensors that disappear by natural processes of bioresorption offer advantages in this context, by eliminating the costs and risks associated with retrieval. A class of bioresorbable pressure sensor that is capable of operational lifetimes as long as several weeks and physical lifetimes as short as several months, as combined metrics that represent improvements over recently reported alternatives, is presented. Key advances include the use of 1) membranes of monocrystalline silicon and blends of natural wax materials to encapsulate the devices across their top surfaces and perimeter edge regions, respectively, 2) mechanical architectures to yield stable operation as the encapsulation materials dissolve and disappear, and 3) additional sensors to detect the onset of penetration of biofluids into the active sensing areas. Studies that involve monitoring of intracranial pressures in rat models over periods of up to 3 weeks demonstrate levels of performance that match those of nonresorbable clinical standards. Many of the concepts reported here have broad applicability to other classes of bioresorbable technologies.

1. Introduction

Excessive pressures within internal cavities of the body can follow from various disease states and/or from responses to physical injuries. Monitoring these pressures is therefore often an indispensable aspect of assessing patient health.[1–3] Specifically, tracking pressures in the brain, eyes, bladder, muscles, and blood vessels can be essential in diagnosing, monitoring, and treating conditions that range from traumatic brain injury (intracranial pressure) to glaucoma (intraocular pressure) and hypertension (blood pressure). The intracranial pressure can change due to fluctuations in the circulatory dynamics of the cerebral blood and cerebrospinal fluid. Surveillance of the pressure in this context usually involves an invasive transducer, inserted by surgical means.[4] Information from such sensors can guide

Q. S. Yang, T.-L. Liu
Department of Mechanical Engineering
Center for Bio-Integrated Electronics
Northwestern University
Evanston, IL 60208, USA

Prof. S. Lee
Department of Chemical Engineering
Konkuk University
Seoul 05029, Republic of Korea

Dr. Y. Xue
Department of Mechanical Engineering
Northwestern University
Evanston, IL 60208, USA

Dr. Y. Yan, Dr. M. R. MacEwan, Prof. W. Z. Ray
Department of Neurological Surgery
Washington University School of Medicine
St Louis, MO 63110, USA
E-mail: rayz@wustl.edu

The ORCID identification number(s) for the author(s) of this article can be found under https://doi.org/10.1002/adfm.201910718.

DOI: 10.1002/adfm.201910718

Prof. S.-K. Kang
Department of Materials Science and Engineering
Seoul National University
Seoul 08826, Republic of Korea

Dr. Y. J. Lee
Department of Materials Science and Engineering
Korea Advanced Institute of Science and Technology (KAIST)
Daejeon 34141, Republic of Korea

Dr. S. H. Lee
Department of Chemical and Biomolecular Engineering
Korea Advanced Institute of Science and Technology (KAIST)
Daejeon 34141, Republic of Korea

Dr. M.-H. Seo, Dr. D. Lu, Dr. J. Koo
Center for Bio-Integrated Electronics
Northwestern University
Evanston, IL 60208, USA

R. T. Yin
Department of Biomedical Engineering
The George Washington University
Washington, DC 20052, USA

decisions on patient care following traumatic brain injury, to protect against permanently damaging physiological events, minimize secondary insults, and optimize intrinsic regenerative processes.[5] Conventional technologies, however, require a second surgical procedure for device extraction after the patient emerges from a period of risk.[6] Furthermore, these devices can elicit immune-mediated inflammatory responses and they can form focus areas for infections.[7,8]

Bioresorbable electronic systems generally, and pressure sensors specifically, can be attractive for these and other clinical scenarios that rely on temporary implants. Here, bioresorbable constituent materials minimize inflammatory responses and eliminate the need for secondary surgical extraction.[9–13] Recent examples include not only pressure but also temperature sensors for the intracranial space;[14–16] photonic devices for monitoring physiological status and neural activity;[17] wireless electronic systems for neuroregenerative therapy;[18] platforms for spatiotemporal mapping of electrical activity from the cerebral cortex;[19] drug release vehicles for infection abatement;[20] and systems for measuring blood flow.[21] Realizing consistent performance throughout a clinically relevant monitoring period with devices that bioresorb completely over slightly longer timescales represents an important goal. Immediately after implantation, surrounding biofluids begin to hydrolyze and dissolve the constituent materials, as an intrinsic feature of the bioresorbable designs. A significant challenge is that bioresorbable encapsulation layers based on most polymers (poly(lactic-*co*-glycolic acid) (PLGA),[22] silk fibroin,[9,20] collagen,[23] and polyanhydride[14]) and inorganic materials (silicon dioxide,[14,24] silicon nitride,[24] and various metal oxides[25] formed by chemical or physical vapor deposition) do not perform well as biofluid barriers to prevent premature and/or uncontrolled degradation of the active elements. Recent reports demonstrate promising results with ultrathin layers of silicon dioxide formed by thermal growth on the surfaces of silicon wafers (t-SiO_2).[15,26,27] A drawback, however, is that the rate of dissolution of t-SiO_2 is extremely slow (dissolution rate of 10^{-3}–10^{-1} nm d^{-1}[15,26]), such that even at thicknesses of a few hundred nanometers, complete dissolution requires timescales of years, typically orders of magnitude longer than clinically relevant operational requirements. Reducing the thicknesses to tens of nanometers can reduce these timescales, but at the expense of increased mechanical fragility. By contrast, lightly doped monocrystalline silicon, which is also impermeable to water,[28,29] dissolves at a comparatively high rate (50–100 nm d^{-1}), to yield dissolution times that are in the range of weeks or months for layers with thicknesses in the micron range. Here, the problem is that the dissolution itself can lead to drifts in sensor performance, at levels that can be significant over timeframes of interest.

This article presents a collection of materials, mechanical design concepts, and multisensor designs that addresses these challenges. The result is a bioresorbable intracranial pressure monitoring platform that offers both stable operation and relatively fast dissolution kinetics, as demonstrated in evaluations using rat models. The principal design features include: 1) sheets of monocrystalline silicon as flexible encapsulation layers that are impermeable to biofluids and are bioresorbable at rates significantly higher than those of alternative barrier materials; 2) optimized architectures, guided by theoretical modeling and finite element analysis (FEA) and validated by experimental measurements, for which the sensor response remains unchanged during the dissolution of the encapsulation layer; 3) tailored formulations of natural wax materials as effective edge-sealing barriers; 4) integrated components for assessing the onset of water penetration into the active areas of the devices. Accurate measurements of intracranial pressures in rats for up to 3 weeks illustrate excellent performance characteristics in devices that adopt these materials and design principles. Taken together, the resulting technology offers an interesting set of capabilities for applications in pressure monitoring not only for traumatic brain injury, but also for other conditions where pressure is an important parameter. The underlying concepts may have additional utility for various types of bio-integrated, bioresorbable sensors.

2. Results and Discussion

2.1. Materials, Designs, Fabrication Procedures, and Dissolution Behavior

Figure 1a presents a schematic illustration of a suspended multilayer membrane (thickness: ≈26.7 μm) sealed over an air-filled cavity (2.4 mm × 2 mm × 60 μm) on a magnesium substrate (6 mm × 8 mm × 100 μm), as the pressure-sensitive structure. The multilayer includes a uniform, lightly doped (boron-doped; doping concentration level: 10^{15}–10^{16} cm^{-3}; resistivity: 8.5–11.5 Ω cm) micromembrane of monocrystalline Si (Si MM; 4 mm × 4 mm × 1.5 μm), a uniform layer of PLGA (65:35 (lactide:glycolide) composition; 6 mm × 8 mm × 16.7 μm), a patterned, highly doped (boron-doped; doping concentration level: ≈10^{20} cm^{-3}; resistivity: 5 × 10^{-4} Ω cm) nanomembrane of monocrystalline Si (Si NM; thickness: ≈200 nm; serpentine length: 1 mm; width: 5 μm; turns: 4; additional details in Figures S1b and S2a, Supporting Information) and another uniform layer of PLGA (6 mm × 8 mm × 8.3 μm). The inset in the bottom left highlights the flexibility of the Si MM/PLGA bilayer (thickness: ≈16.7 μm). Here, the silicon serves as a bioresorbable barrier to biofluid penetration. An optical micrograph in the bottom right inset (red) shows the serpentine

Prof. Y. Huang
Departments of Civil and Environmental Engineering
Mechanical Engineering
Materials Science and Engineering
Center for Bio-Integrated Electronics
Northwestern University
Evanston, IL 60208, USA
E-mail: y-huang@northwestern.edu
Prof. J. A. Rogers
Departments of Materials Science and Engineering
Biomedical Engineering
Neurological Surgery, Chemistry Mechanical
Engineering Electrical Engineering
and Computer Science
Center for Bio-Integrated Electronics
Simpson Querrey Institute, and Feinberg School of Medicine
Northwestern University
Evanston, IL 60208, USA
E-mail: jrogers@northwestern.edu

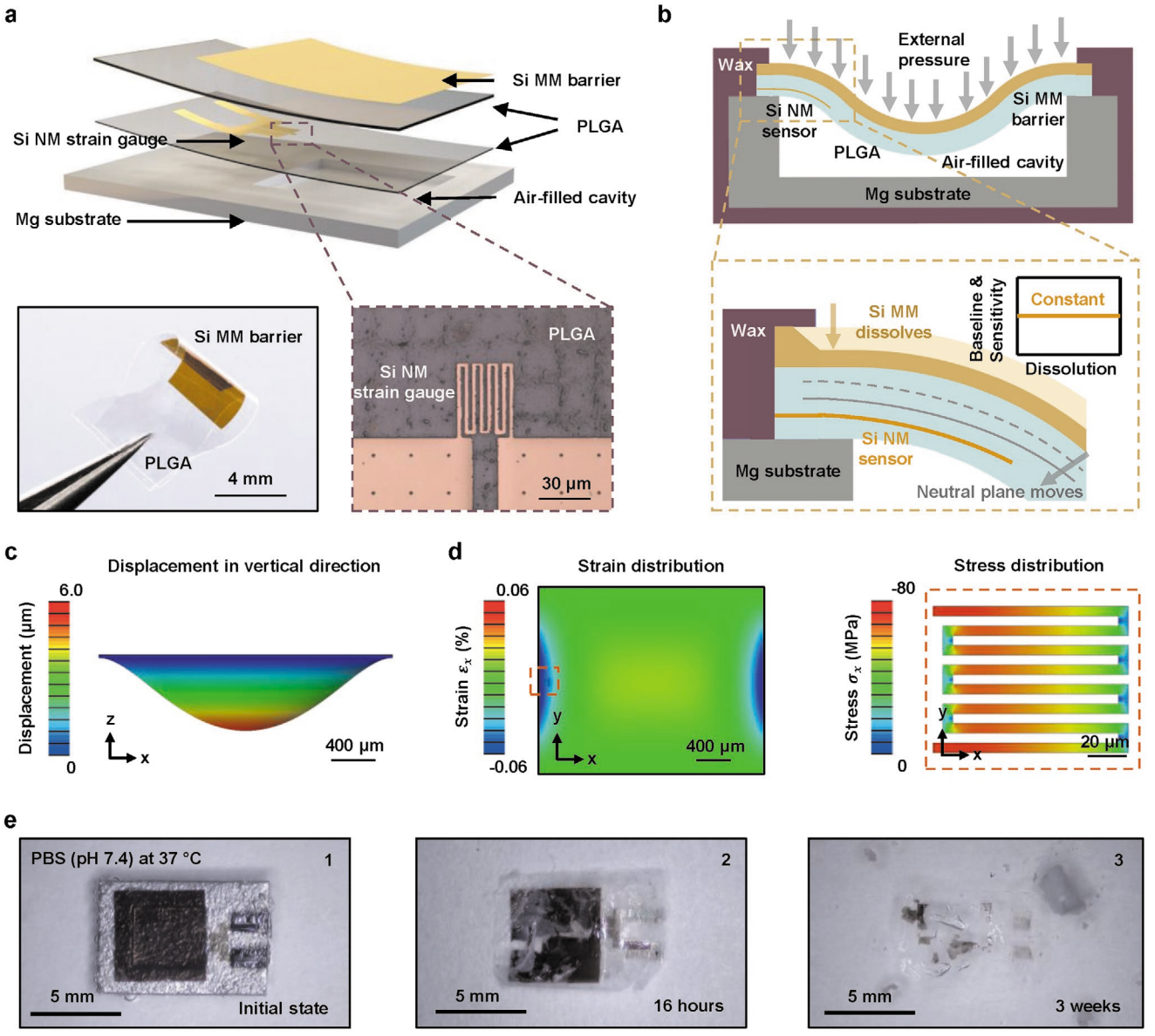

Figure 1. Materials, device architectures and dissolution behavior of a bioresorbable pressure monitoring system with stable operation and subsequent fast dissolution. a) Schematic illustration of a suspended, multilayer membrane (thickness: ≈26.7 μm) sealed over an air-filled cavity (2.4 mm × 2 mm × 60 μm) on a magnesium substrate (6 mm × 8 mm × 100 μm), as the pressure-sensitive structure. The multilayer includes a uniform micromembrane of monocrystalline lightly doped Si (Si MM; 4 mm × 4 mm × 1.5 μm) as a top water barrier, a uniform layer of PLGA (6 mm × 8 mm × 16.7 μm) as an adhesive interlayer, a patterned nanomembrane of monocrystalline doped Si (Si NM; thickness: ≈200 nm; serpentine length: 1 mm; width: 5 μm; turns: 4) as a sensing element and another uniform layer of PLGA (6 mm × 8 mm × 8.3 μm) as another adhesive interlayer. Bottom left inset: Optical image of a flexible Si MM biofluid barrier (4 mm × 4 mm) on a PLGA substrate (thickness: 16.7 μm). Red right inset: Optical microscope image of the serpentine structure of the Si NM that forms the strain gauge, bonded on a layer of PLGA (thickness: 8.3 μm) that lies over a trench etched into the surface of the Mg substrate. b) Schematic cross-sectional illustration of the working principle during dissolution. The thickness and rate of dissolution of the impermeable Si MM define the functional lifetime. The patterned Si NM offers a piezoresistive response to bending strains that result from differences between the pressure of the surroundings and that of the air trapped inside the cavity. Bottom inset: The thickness of the Si MM decreases monotonically with time of immersion due to a process of surface erosion by hydrolysis, thereby reducing its bending stiffness and, at the same time, moving the location of the neutral plane associated with bending of the entire multilayer stack. Careful mechanics designs balance these two time-dependent, but time-synchronized, parameters to avoid any drift in sensitivity. c) Fundamental mechanisms of pressure sensing captured by 3D finite element analysis under an applied pressure of 15 mmHg: the vertical movements of the multilayer in a cross-sectional view, and d) the strain and stress distributions along the *x*-direction of the multilayer and Si NM strain gauge, respectively. e) Stages of dissolution of a device without wax immersed in PBS (pH 7.4) at 37 °C, as an approximation of a physiological environment.

structure of the Si NM that forms the strain gauge, bonded on a layer of PLGA that lies over a trench etched into the surface of the Mg. The schematic cross-sectional illustration in Figure 1b highlights the working principle of the system during dissolution. The Si MM on top protects the sensing element from exposure to biofluids; its thickness and rate of

dissolution define the functional lifetime. The patterned Si NM offers a piezoresistive response to bending strains that result from differences between the pressure of the surroundings and that of the air trapped inside the cavity. The PLGA layers bond the various components to yield an air-tight seal. A mixture of natural wax materials (thickness: ≈300 μm) forms biofluid barriers to prevent penetration along the edges of the structure. The experimental section describes the fabrication processes in detail. Table S1 (Supporting Information) presents key features and performance attributes of this sensor compared with existing devices.[14–16,30,31]

3D finite element analysis quantitatively captures the fundamental mechanisms of pressure sensing. Figure 1c shows the vertical movements in a cross-sectional view for an applied pressure of 15 mmHg, within a range relevant to intracranial monitoring. The maximum displacement occurs in the center of the suspended film, provided that the depth of the trench exceeds this displacement. The piezoresistive response of the Si NM strain gauge mainly depends on the stress along the *x*-direction, shown in Figure 1d. The maximum strain along this direction for any applied pressure across the range of interest occurs at the edge of the trench, coincident with the location of the strain gauge (Figure S2c, Supporting Information). Extending the length of the gauge over the air-filled cavity reduces the overall sensitivity (Figure S2e,f, Supporting Information). The resistance of the gauge changes with pressure in a linear fashion with a slope of ≈17 Ω $mmHg^{-1}$, to define a metric for sensitivity, $S = \Delta R/\Delta P$. Reducing the thickness of the PLGA interlayers (Figure S3, Supporting Information) or the Si NM for the strain gauge, extending the trench area and depth (Figure S4, Supporting Information), and increasing grid numbers in strain gauge are options for improving the sensitivity. The total size and weight of the device without the natural wax edge encapsulation are 4 mm × 7 mm × 0.13 mm (trench size: 2.4 mm × 2 mm × 0.06 mm) and ≈20 mg, respectively. Figure S2c (Supporting Information) shows a device on a golf ball to illustrate the dimensions.

Immediately after implantation, surrounding biofluids begin to hydrolyze and dissolve the various materials in these devices, starting with the Si MM. The thickness decreases monotonically with time of immersion due to a process of surface erosion by hydrolysis, thereby reducing its bending stiffness and, at the same time, moving the location of the neutral plane associated with bending of the entire multilayer stack. The reduction in bending stiffness increases the sensitivity of the device to pressure, while the corresponding motion of the neutral plane toward the Si NM strain gauge has the opposite effect. Specifically, for a given pressure, the response is proportional to the ratio of the bending stiffness to the distance between the sensing position and the neutral plane. Engineering an appropriate ratio for these two time-dependent, but time-synchronized, parameters provides a means to design devices that avoid any drift in sensitivity throughout the dissolution of the Si MM, as discussed in detail subsequently.

Figure 1e presents the stages of dissolution of a device without wax encapsulation, upon immersion in phosphate-buffered saline (PBS, pH 7.4) at 37 °C, as an approximation of a physiological environment. The end state corresponds to complete disappearance of the device and all of the constituent materials. The magnesium substrate disintegrates into small clusters and fully dissolves within 16 h based on a hydrolysis reaction, $Mg + 2H_2O \rightarrow Mg(OH)_2 + H_2$. PLGA degrades by hydrolysis of its ester linkages to the corresponding monomers, lactic acid and glycolic acid, both of which are natural by-products of various metabolic pathways in the body. Before complete hydrolysis, water permeation into the PLGA leads to swelling and associated fracture of the Si MM encapsulation and the Si NM strain gauge. After 3 weeks, the PLGA dramatically degrades into several wrinkled pieces. At this stage, only residual amounts of material from the Si MM encapsulation, Si NM strain gauge and the W contact pads remain, with complete dissolution within 4 weeks ($Si + 4H_2O \rightarrow Si(OH)_4 + 2H_2$; $W \rightarrow W^{4+}$, W^{5+}, and W^{6+}). These timescales are consistent with those separately reported for each of the constituent materials: Mg, W, lightly doped Si, and highly doped Si dissolve at rates of 50–100 μm d^{-1} (largely affected by the initial oxidation on the surface), 100–250 nm d^{-1}, 50–100 nm d^{-1}, and 5–10 nm d^{-1}, respectively.[14,28,29,32] Increasing the thicknesses of the Si MM and PLGA interlayers, the doping concentration of the Si MM and/or the ratio of lactic acid in the PLGA will increase the respective times.

2.2. Strategies for Edge Encapsulation Using Natural Wax Materials

Robust, water-proof seals along the edges of the device are critically important in achieving stable operation. Here, the encapsulation prevents the penetration of biofluids through these regions and the associated film interfaces to protect the strain gauge element, the contact pads and other sensitive components. In addition to impermeability to water, the material for edge encapsulation must provide compliant contact and strong, reliable conformal bonding to the other materials. The mechanical fragility of inorganic films and the difficulty of depositing thick, conformal coatings limit their utility for this purpose. Conventional biodegradable polymers, such as PLGA, silk fibroin, collagen, polyanhydride and others tend to swell due to water uptake, in a manner that can lead to delamination and disassembly. Natural wax and wax-based materials offer superior properties.

Figure 2a explains the procedures for assembling a device and forming wax encapsulation around the edges and top perimeter regions, including 1) aligning the serpentine geometry of the Si NM strain gauge with a film of PLGA (thickness: ≈8.3 μm) near the boundary of the etched trench on the Mg substrate (Figure S2c, Supporting Information), followed by heating to temperatures slightly greater than the T_g of the PLGA to seal the air-filled cavity, 2) transferring a Si MM layer with another film of PLGA (thickness: ≈16.7 μm) on top, centered over the trench and heating to temperatures over T_g of the PLGA to facilitate bonding, 3) placing a thin piece of poly(dimethylsiloxane) (PDMS; part A:part B = 4:1; 3 mm × 3 mm × 0.5 mm) with a slightly tacky surface and with lateral dimensions smaller than this membrane but larger than the trench, onto the top surface to protect the central region of the Si MM, 4) immersing the entire structure in melted wax for several seconds, followed by removal to form a coating of wax (thickness of 290 ± 40 μm measured by a stylus profilometer; $N = 10$) across the entire

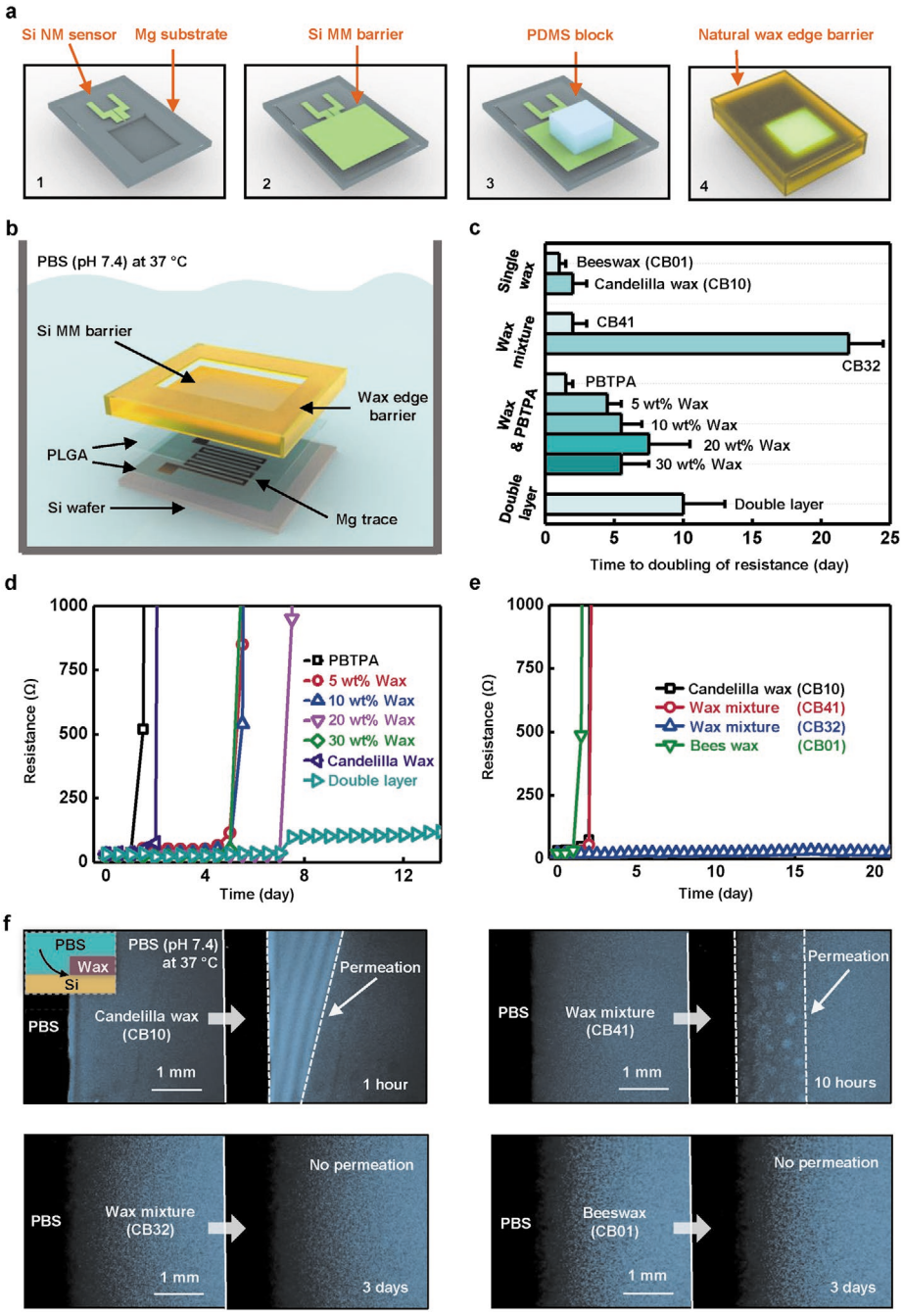

Figure 2. Strategies for edge encapsulation using natural wax materials. a) Procedures for assembling a device and forming wax encapsulation around the edges and top perimeter regions, including (1) aligning the serpentine geometry of the Si NM strain gauge with a film of PLGA (thickness: 8.3 μm) near the boundary of the etched trench on the Mg substrate, (2) transferring a Si MM layer with another film of PLGA (thickness: ≈16.7 μm) on top, centered over the trench, (3) placing a piece of thin, tacky PDMS (3 mm × 3 mm × 0.5 mm) with lateral dimensions smaller than this membrane but larger than the trench onto the top surface to protect the central region of the Si MM, (4) immersing the entire structure in melted wax for several seconds and then removing it to form a coating of wax (thickness of ≈ 300 μm) across the entire structure, and removing the PDMS with wax on the top while the structure is still warm, to expose the central part of the Si MM. b) Schematic illustration of an experimental set-up designed to test water penetration through a full encapsulation structure associated with immersion in PBS (pH 7.4) at 37 °C. A patterned thin film trace of Mg (thickness: 300 nm; serpentine length: 1.45 mm; width: 150 μm; turns: 4) formed on a silicon wafer coated with PLGA (thickness: 8.3 μm) serves as an indicator for water penetration. c) Average times for the resistance to double ($\Delta R/R_0 \geq 100\%$; $N = 3$) with various formulations of wax-based materials as edge barriers, including single wax (CB01 and CB10), wax mixture (CB41 and CB32), PBTPA with wax (weight ratio of Candelilla wax in PBTPA: 0, 5, 10, 20, and 30 wt%), and bilayer wax (inside layer: PBTPA with 20 wt% Candelilla wax; outside layer: CB01). The thicknesses in all cases are ≈300 μm. d,e) Representative curves showing changes in resistance of Mg traces as a function of soaking time for structures protected by various wax edge barriers. f) Optical micrographs illustrating water penetration along the Si–wax interface for various wax materials (CB10, CB41, CB32, and CB01, respectively). A layer of wax (≈300 μm) lies on the right half area of a silicon wafer (2 cm × 1 cm × 0.525 mm) immersed in PBS (pH 7.4) at 37 °C. Top left inset: Schematic illustration of the experimental set-up. The thicknesses of wax materials in all cases are ≈300 μm.

structure, and 5) eliminating the PDMS with wax on top, to expose the central part of the Si MM. The PLGA layer bonds to the Mg substrate to yield an air-tight seal, thereby preventing leakage of wax into the cavity during formation of the edge encapsulation. The total size of the device with the natural wax edge encapsulation is ≈4.6 mm × 7.6 mm × 0.73 mm.

Beeswax (CB01) and Candelilla wax (CB10) are two natural materials reported recently for applications in bioresorbable electronics.[33] Beeswax contains hydrocarbons (14%), monoesters (35%), diesters (14%), triesters (3%), hydroxy monoesters (4%), hydroxy polyesters (8%), acid esters (1%), acid polyesters (2%), free fatty acids (12%), free fatty alcohols (1%), unidentified constituents (6%).[34] Candelilla wax includes hydrocarbons (about 50%, chains with 29–33 carbons), esters of higher molecular weight (20–29%), free acids (7–9%), and resins (12–14%, mainly triterpenoid esters).[35] Beeswax possesses less hydrocarbon content and more ester and anhydride derivatives than Candelilla wax. Hydrolysis of ester and anhydride derivatives in these biocompatible and bioresorbable materials leads to dissolution on timescales of several months in vivo, as described in previous publications.[33,36] The swelling ratio of natural wax increases with the amount of these derivatives. The water uptake in Beeswax tends to be larger than that in Candelilla wax. Nevertheless, Candelilla wax is comparatively brittle, to an extent that can often lead to cracks in the wax and at interfaces with other materials.

Mixing Candelilla wax with Beeswax provides a route to balance these considerations. Formulations denoted as CB10, CB41 (ratio of Candelilla wax to Beeswax: 4:1), CB32 (ratio: 3:2) and CB01 fracture at the flexural strain (stress) of 0.98% (7.57 MPa), 1.60% (6.88 MPa), 3.41% (6.51 MPa) and 29.00% (0.98 MPa) under a three-point bending test (Figure S5, Supporting Information), respectively. Mixing Candelilla wax with a biodegradable polymer (polyanhydride, PBTPA) further enhances the mechanical properties. Energy-dispersive X-ray spectroscopy (EDAX) reveals no phase separation between the PBTPA and wax, as in Figure S6 (Supporting Information). The addition of wax to PBTPA increases the hydrophobicity and lowers the surface energy as well (Figure S7, Supporting Information).

Figure 2b illustrates an experimental set-up designed to test the behavior of a fully encapsulated structure upon immersion in PBS (pH 7.4) at 37 °C. A patterned thin film trace of Mg (thickness: 300 nm; serpentine length: 1.45 mm; width: 150 μm; turns: 4) formed on a silicon wafer coated with PLGA (thickness: 8.3 μm) provides an indicator for water penetration. Here, the resistance of the Mg trace increases due to hydrolysis: $Mg + 2H_2O \rightarrow Mg(OH)_2 + H_2$. An overcoat of PLGA (thickness: 16.7 μm) serves as a supporting surface for a Si MM encapsulation layer (thickness: ≈1.5 μm). For CB10, CB41, CB32, and CB01, immersion in melted wax at 80 °C for 5 s with a piece of PDMS on top of the Si MM results in an edge encapsulation (thickness: ≈300 μm). Removing the PDMS leaves the central region of the Si MM exposed, as described previously. Shrinkage of natural wax during solidification (12.0%, 12.1%, 12.7%, and 13.3% for CB10, CB41, CB32, and CB01, respectively; Figure S8, Supporting Information) requires care to ensure conformal contact around the edges and to avoid cracking of the Si MM. Wax formulations with PBTPA (PBTPA added with 0, 5, 10, 20, and 30 wt% Candelilla wax, denoted as PH0, PH5, PH10, PH20, and PH30, respectively) involve exposure to ultraviolet light to induce crosslinking, as a final step. Previous studies demonstrate that monocrystalline Si membranes are perfect water barriers for timescales shorter than those required for hydrolysis to consume the silicon.[28,29,37,38] As a result, changes in the resistances of the Mg traces in these experiments result from passage of water through the wax composite material, and then through the PLGA and the interfaces with the silicon.

Figure 2c presents the average times for the resistances of the Mg traces to double ($\Delta R/R_0 \geq 100\%$). Representative curves that show changes in resistance as a function of soaking time for structures protected by various wax edge barriers appear in Figure 2d,e. In all cases, the thickness of one layer of wax is roughly 300 μm. These times for PH0, PH5, PH10, PH20, and PH30 are 2, 4, 5, 7, and 5 d, respectively. Increasing the concentration of Candelilla wax in PBTPA from 0 to 20 wt% increases the average time. The mechanical properties of PH30 are, however, inferior to those of PH20, resulting in a decrease in the average time, largely due to poor interfacial adhesion. Additional details are in Figure 2f. Bilayers of CB10/PH20 yield times of 10 d, slightly longer than those for PH20 alone. For a single layer of pure wax, i.e., Beeswax wax (CB01) or Candelilla wax (CB10), the average times are only 2 d. The results of CB41 are similar to those of CB10, indicating that the addition of 20% Beeswax into Candelilla wax yields no significant improvement in the barrier properties. The CB32 material yields resistances that do not change for up to 22 d, 10 times longer than that of the other wax mixtures examined here.

Previous studies indicate that Candelilla wax as a planar encapsulation layer can protect Mg resistors for up to 10 d. Use in edge encapsulation involves significant additional challenges in conformal coverage, strong bonding and other effects that collectively result in an average time of only 2 d. Here, the primary path for water penetration is at the interface between the Si MM and the Candelilla wax. Optical micrographs in Figure 2f illustrate the effect for various wax materials (CB10, CB41, CB32, and CB01, respectively). A layer of wax (≈300 μm), deposited using the same techniques described previously, lies on the right half area of a silicon wafer (2 cm × 1 cm × 0.525 mm). Images as viewed from the top of the experimental set-up shown in the top left inset highlight the penetration of water along the interface between the silicon and the wax, for immersion in PBS (pH 7.4) at 37 °C. The water at the interface results mainly from interfacial penetration as opposed to diffusion through the wax within 3 d, based on results from experiments with the Mg traces. For the case of CB10 (more details shown in Figure S9a, Supporting Information), penetration occurs on the edge within 15 min. Afterward, water penetrates at a rate of 6 mm h^{-1} along the direction perpendicular to the edge, as determined by analyzing the penetration length at different soaking durations. For CB41 (more details shown in Figure S9b, Supporting Information), the penetration appears on the edge at ≈10 h, and progresses at a rate of 0.4 mm h^{-1}. The nonuniform pattern of penetration in this case largely results from the higher level of water uptake for Beeswax compared with Candelilla wax. CB32 and CB01 present no discernible water penetration at the interface within 3 d.

These results suggest that the addition of Beeswax in the wax mixture reduces the rate of water penetration at the interface, likely due partly to the increased amount of hydrogen bonding associated with the ester and anhydride derivatives and partly to the improved ductility and reduced hardness. These and previously reported findings indicate that although Candelilla wax has low water permeability, its poor interface properties with Si limit its effectiveness as an encapsulation layer. By contrast, Beeswax offers improved interface properties but it has relatively high water permeability. Mixing Candelilla wax and Beeswax provides a balance of these considerations, to yield superior performance. For all cases, increasing the thickness or using multilayer constructs can yield further improvements.

2.3. Mechanical Designs and Strategies for the Top Encapsulation

Pristine, defect-free coatings of inorganic materials can serve as excellent water barriers. Monocrystalline Si membranes and t-SiO_2 layers represent two particularly successful examples. The hydrolysis of thin films of t-SiO_2 in physiological conditions occurs at a rate of 10^{-3}–10^{-1} nm d^{-1}, which leads to times for dissolution (e.g., years for films with submicron thicknesses) that substantially exceed those that are ideal for most applications in biomedicine. The comparatively rapid rate (50–100 nm d^{-1}) of dissolution for undoped, or lightly doped, monocrystalline Si (e.g., days or weeks for films with submicron thickness) represents an advantage in this context. A key design challenge is in avoiding drift in the operational characteristics of the device as the Si MM encapsulation dissolves and its thickness decreases continuously (**Figure 3**a). This thickness decrease changes the response of the underlying pressure sensor by altering the total bending stiffness. Figure 3b presents the calculated maximum displacements of the suspended film for applied pressures across the range of interest for different thicknesses of the Si encapsulation. The displacement variation of the suspended film under the same applied pressure during dissolution is consistent with the expected change of the total bending stiffness. The maximum displacement increases as the thickness decreases due to dissolution, as a result of corresponding reductions in the bending stiffness. For instance, the maximum displacements at 20 mmHg with 1.5, 1.0, and 0.5 μm of Si MM encapsulation are 7.8, 8.6, and 10.3 μm, respectively.

Besides the alteration of the total bending stiffness, the thickness decrease of the encapsulation also induces shifts of the neutral plane position in the suspended multilayer. Carefully configured layouts can balance these two competing effects precisely to avoid any change in the response of the sensor as the silicon dissolves. Specifically, the stress response under applied pressure, that is, the sensitivity, is linearly proportional to 1) distance from the sensing element to the neutral plane $h_{\text{neutral}} - z_{\text{sensor}}$, and 2) inverse of total bending stiffness of the diaphragm EI_{total}, which can be written as

$$\frac{\bar{\sigma}}{\Delta P} \propto \frac{\left(h_{\text{neutral}} - z_{\text{sensor}}\right)}{EI_{\text{total}}} \tag{1}$$

where $\bar{\sigma} = (\sigma_x + \sigma_y)$. In the bioresorbable pressure sensor system, the encapsulation h_{encap}(≈1.5 μm) is much smaller than the bottom PLGA thickness h_{PLGA}(≈25 μm), and Equation 1 can be further written out as

$$\frac{\bar{\sigma}}{\Delta P} \propto \left[\frac{1 - 2\frac{z_{\text{sensor}}}{h_{\text{PLGA}}} + \left(2 - 2\frac{z_{\text{sensor}}}{h_{\text{PLGA}}}\right)\frac{E'_{\text{Si}}\, h_{\text{encap}}}{E'_{\text{PLGA}}\, h_{\text{PLGA}}}}{1 + 4\frac{E'_{\text{Si}}\, h_{\text{encap}}}{E'_{\text{PLGA}}\, h_{\text{PLGA}}}} \right] \tag{2}$$

Here the plane strain modulus $E'_{\text{PLGA}} = \frac{E_{\text{PLGA}}}{1 - \nu_{\text{PLGA}}^2}$, $E'_{\text{Si}} = \frac{E_{\text{Si}}}{1 - \nu_{\text{Si}}^2}$, where E_{PLGA}, E_{Si}, ν_{PLGA}, ν_{Si} are the moduli and Poisson's ratios of PLGA and Si, respectively. When $z_{\text{sensor}}/h_{\text{PLGA}} = 1/3$, Equation 2 becomes a constant and no longer depends on h_{encap}, thereby resulting in constant sensitivity during the dissolution of monocrystalline silicon encapsulation.

The analytical results from Equation 2 (line) and simulation results from FEA (scatter) for the sensitivity variation as a function of the percentage dissolution of the Si encapsulation appears in Figure 3a, with different relative sensing positions of the strain gauge ($z_{\text{sensor}}/h_{\text{PLGA}} = 1/2$, 1/3, and 1/4) in the PLGA. The schematic illustration at the bottom shows the reduction of encapsulation thickness and the corresponding shift of the neutral plane during dissolution. The results reveal that the sensitivity drops by 90% at 1/2, 80% at 1/5 and 60% at 1/10 of the encapsulation thickness when the Si NM strain gauge is in the middle of the PLGA layer ($z_{\text{sensor}}/h_{\text{PLGA}} = 1/2$). The bottom quarter position ($z_{\text{sensor}}/h_{\text{PLGA}} = 1/4$) leads to an increase of sensitivity by 105% at 1/2, 110% at 1/5 and 120% at 1/10 of the encapsulation thickness. Surprisingly, the one-third position of strain sensor in PLGA layer results in a constant sensitivity during the entire process of dissolution. Figure 3c shows the difference in sensitivity as a relationship with the change in the encapsulation thickness, determined by simulation, for relative sensing positions $z_{\text{sensor}}/h_{\text{PLGA}}$ from 0 to 1/2. The sensitivity is constant at the one-third position (1/3). For cases above (from 1/3 to 1/2) and below (from 0 to 1/3) this position, the sensitivity tends to decrease and increase, respectively. The magnitude of the increase grows as the sensor position approaches the bottom surface of the PLGA. The initial sensitivity also depends on the relative sensing position (Figure S2d, Supporting Information). The maximum occurs at the bottom position and decreases as the position moves upward in the PLGA layer as expected, due to corresponding reductions in bending stresses.

As mentioned previously, dissolution of Si produces silicic acid ($Si(OH)_4$), due to the hydrolysis reaction $Si + 4H_2O \rightarrow Si(OH)_4 + 2H_2$. Figure 3d shows the kinetics of dissolution, evaluated by reductions of the overall thickness in PBS (pH 7.4) at 37 °C, corresponding to a rate of 54 ± 7 nm d^{-1}. Full dissolution occurs on day 28, consistent with requirements in ICP monitoring (3–4 weeks). Increasing the doping concentration and/or the thickness can increase the time to full dissolution.

Tests of the pressure response involve a syringe partially filled with PBS (pH 7.4) at 37 °C to control the pressure across a range relevant to the intracranial cavity (0–20 mmHg). A bioresorbable sensor constructed with the strain gauge at the 1/3 position lies in the barrel of the syringe, along with a commercial sensor.

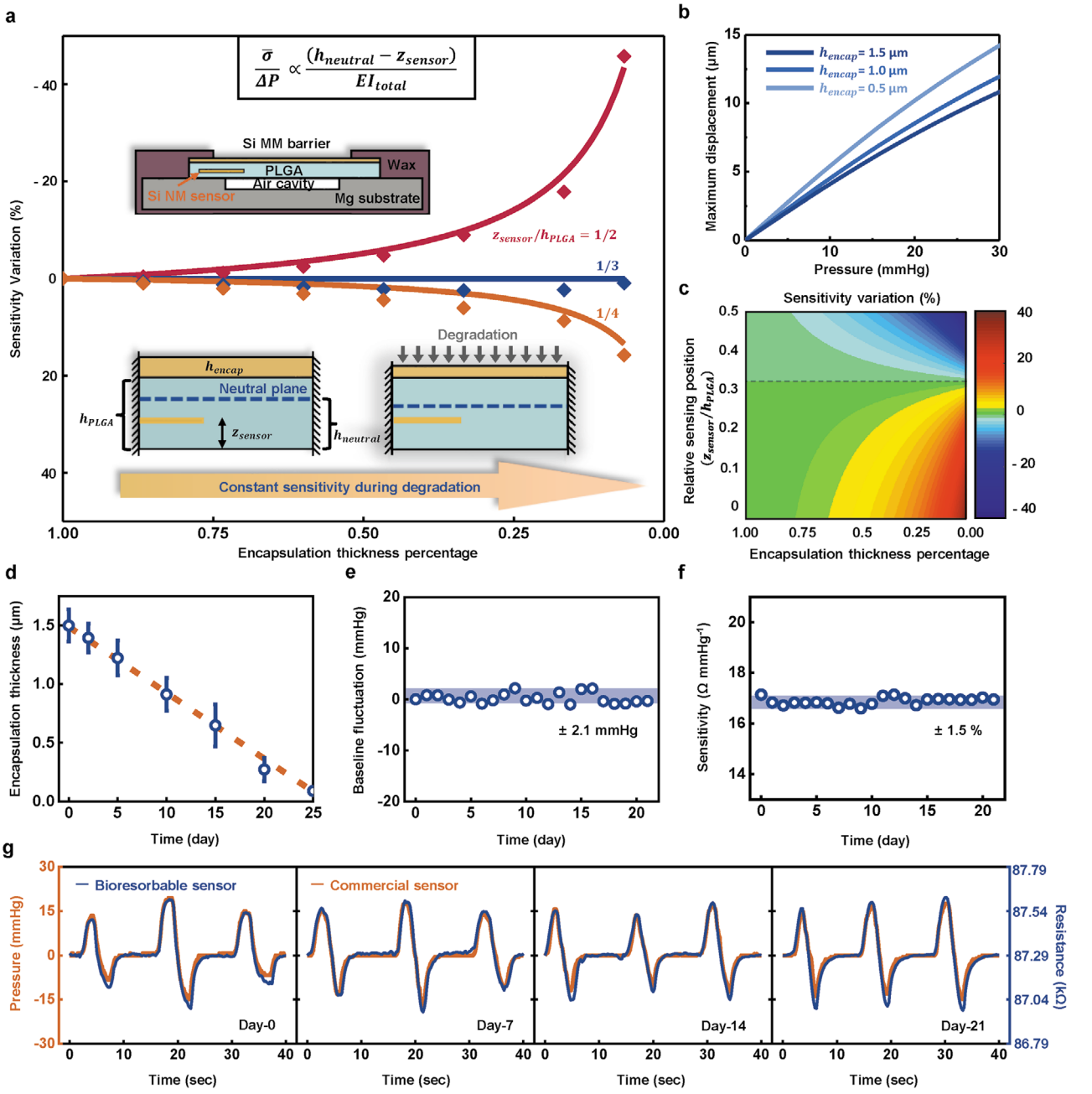

Figure 3. Mechanical designs and strategies for Si MM top encapsulation. a) Analytical (line) and simulated (scatter) results for the change in sensitivity as a function of the percentage dissolution of the Si encapsulation with different relative positions of the strain gauge (z_{sensor}/h_{PLGA} = 1/2, 1/3, and 1/4) in the PLGA. Bottom inset: Schematic illustration showing the reduction of the encapsulation thickness and the corresponding movement of the neutral plane during dissolution. The response to applied pressure is proportional to the ratio of these two parameters: (1) distance from the sensing element to the neutral plane $h_{neutral} - z_{sensor}$, and (2) total bending stiffness of the diaphragm EI_{total}. The results reveal that the sensitivity drops by 90% at 1/2, 80% at 1/5, and 60% at 1/10 of the encapsulation thickness when the Si NM strain gauge is in the middle of the PLGA layer (z_{sensor}/h_{PLGA} = 1/2). The bottom quarter position of the strain gauge in the PLGA layer (z_{sensor}/h_{PLGA} = 1/4) leads to an increase of sensitivity by 105% at 1/2, 110% at 1/5 and 120% at 1/10 of the encapsulation thickness. The one-third position results in a constant sensitivity during the entire process of dissolution. b) Calculated maximum displacements of the suspended film for applied pressures across the range of interest for different thicknesses of the Si encapsulation. c) Difference in sensitivity as a relationship with the change in the encapsulation thickness, determined by simulation, for relative sensing positions from 0 to 1/2. The sensitivity is constant at the one-third position (1/3). For cases above (from 1/3 to 1/2) and below (from 0 to 1/3) the one-third position, the sensitivity tends to decrease and increase, respectively. d) Kinetics of dissolution, evaluated by reductions of the overall thickness in PBS (pH 7.4) at 37 °C, corresponding to a rate of 54 ± 7 nm d^{-1}. The error bars represent the mean ± S.D. for five measurements. e) Baseline for the bioresorbable device drifts by only ±2.1 mmHg for pressures in the range of 0–20 mmHg in PBS (pH 7.4) at 37 °C for 3 weeks. f) Sensitivity remains 17.3 ± 0.1 Ω mmHg^{-1} in PBS (pH 7.4) at 37 °C for this same 3-week period. g) Comparisons show remarkable consistency in performance between the bioresorbable sensor (blue line) and the commercial sensor (orange line) on day 0, 7, 14, and 21 in PBS (pH 7.4) at 37 °C.

The responses of the bioresorbable and commercial sensors are similar, to within measurement uncertainties, at external pressures up to 100 mmHg, as shown in Figure S10 (Supporting Information), consistent with the clinical standards of the Association for the Advancement of Medical Instrumentation (AAMI) and the American National Standards Institute (ANSI). The results in Figure 3e demonstrate that the pressure evaluated with the bioresorbable device fluctuates by only ±2 mmHg for external pressures in the range of 0– 20 mmHg over 3 weeks, similar to the accuracy for intracranial pressure sensors stipulated in the AAMI. Discussions of the measurement and calculation of baseline fluctuation and sensitivity, and on the differences between applied pressure and external pressure appear in the Supporting Information. The findings summarized in Figure 3f indicate that the sensitivity remains 17.3 ± 0.1 Ω $mmHg^{-1}$ over this same 3-week period. Comparisons show remarkable consistency in performance between the bioresorbable (blue line) and the commercial (orange line) sensors on day 0, 7, 14, and 21, as in Figure 3g. On the basis of the measured rates of dissolution, the thickness of an Si MM in a given device will be, approximately, 1.5, 1.1, 0.75, and 0.35 μm on day 0, 7, 14, and 21, respectively. On day 23, an external pressure of 15 mmHg induced cracks in the Si MM (estimated thickness at this stage, ≈0.25 μm). Subsequent leakage in the air-filled cavity results in a significant reduction in sensitivity (<5 Ω $mmHg^{-1}$). To further prove that the 1/3 location is advantageous compared to other locations, Figure S11 (Supporting Information) demonstrates an experimentally measured reduction of the sensitivity by 28.6% upon reduction of the thickness of Si MM barrier from 1.5 μm (13.3 Ω $mmHg^{-1}$) to 0.2 μm (9.5 Ω $mmHg^{-1}$) for the case of the sensing element at the 1/2 location. These experimental measurements match the numerically simulated reductions of 26.3%. These additional results provide further support for our theoretical analysis of the mechanics and the device response.

2.4. Bioresorbable Indicators of the On-set of Water Penetration

Although the devices can offer stable performance over clinically relevant times, additional components for assessing water penetration can be extremely useful in cases where the edge encapsulation unexpectedly fails or the Si MM layer cracks or other modes of failure arise. Here, the addition of a Mg resistor (thickness: 300 nm; serpentine length: 1.45 mm; width: 150 μm; turns: 4) at the middle position of the PLGA layer underneath the Si MM can serve as a sensor for water penetration, as in the schematic diagram in the upper side of **Figure 4**a. The image highlights the mechanical flexibility with such a sensor included. Figure 4b shows a completed system. Four biodegradable molybdenum wires (Mo, 25 μm diameter; two for the Si NM strain gauge and two for the Mg warning signal) serve as interfaces for data acquisition. Conductive wax (at 175 °C; weight ratio, W microparticles: Candelilla wax = 16:1) placed on the W contact pads for the Si NM strain gauge and on the Mg pads for the Mg traces establish interconnects between the metal wires and the sensors. The inset shows an optical micrograph of the serpentine Mg trace, which lies above the air cavity and away from the Si NM strain gauge. The surrounding black region corresponds to the wax-based edge barrier.

Experiments reveal the sensitivity of the system to changes in pressure with and without the water penetration sensor, as in Figure 4c. In both cases, the resistance changes in a linear fashion with external pressure across the range from 0–20 mmHg, with sensitivities of 16.8 ± 0.2 and 17.3 ± 0.1 Ω $mmHg^{-1}$ for the cases with and without the sensor, respectively. Studies of devices immersed in PBS (pH 7.4) at 37 °C show that the resistance of the strain gauge and the water penetration sensor remain unchanged over 24 d, with an increase in the latter shortly thereafter and complete electrical disconnection by day 26, consistent with water penetration around day 25. From day 25 to day 29, the strain gauge exhibits only a slow increase in resistance, as an ambiguous indication of water penetration that could otherwise be misinterpreted as a change in pressure. After day 29, the resistance increases significantly.

2.5. Long-Term Monitoring of ICP in Animal Models

Demonstrations of the practical utility of the devices involve chronic monitoring of ICP in animal models. All studies followed the recommendations in the Guide for the Care and Use of Laboratory Animals of the National Institutes of Health, the suggestion from the panel of Euthanasia of the American Veterinary Medical Association and, the agreements with the Washington University in St Louis institutional guidelines. All procedures followed the approved protocols by the Institutional Animal Care and Use Committee (IACUC) of Washington University in St Louis (protocol no. 20 170 189). **Figure 5**a presents a diagram of a device on the skull of a rat. An opening on the skull directly underneath the sensing area ensures contact with the cerebrospinal fluid (CSF). Figure 5b shows integration of a measurement and protection unit that interfaces to the sensor and allows the rat to move freely within a cage environment. Affixing the bottom part of this system to the skull using dental cement enables chronic, continuous monitoring of ICP (Figure S12a,b, Supporting Information). The procedures for implantation, consisting of exposing the skull area, opening a craniotomy defect, mounting the sensors above the defect and sealing the cavity with a commercial bioresorbable glue (COSEAL surgical sealant) on the edge, are summarized in Figure 5c. The black inset shows a bioresorbable sensor before implantation. A standard clinical ICP monitor inserted through a second craniotomy defect provides a basis for characterizing the functional period and the lifetime of the bioresorbable sensors.

Figure 4d–g features in vivo recordings captured using a representative device. Data include variations in ICP induced by compressing and releasing the flank of the animal (Figure 5d), by orienting the animal in the Trendelenburg (30° head-down) and reverse Trendelenburg (30° head-up) positions (Figure 5e), and contracting the flank by application of force (Figure S12c, Supporting Information) during a short period (<3 min). In all cases, the measurements compare well to those recorded with the commercial sensor. This level of accuracy remains unchanged for up to 3 weeks, without recalibration (Figure 5f,g). Evaluations of the operational stability in vivo involve measurements of sensitivity and baseline

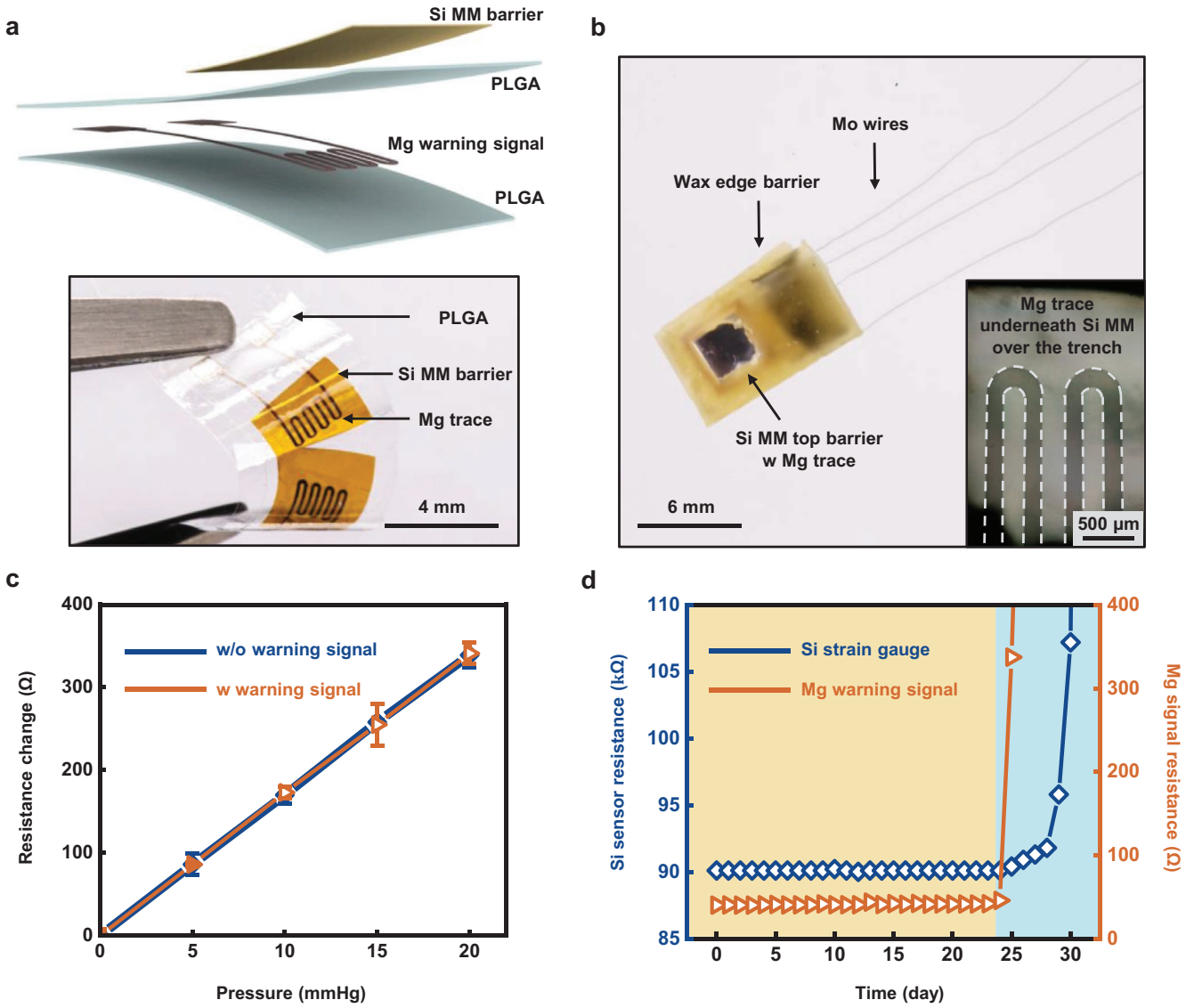

Figure 4. Design strategies and integration of a sensor for the onset of water penetration. a) Schematic illustration of a Mg resistor (thickness: 300 nm; serpentine length: 1.45 mm; width: 150 μm; turns: 4) as a sensor for water penetration located at the middle position of the PLGA layer underneath the Si MM. Bottom inset: Optical image showing the flexibility of the system with such a sensor included. b) Photograph of a bioresorbable pressure sensor with sensor integrated. Four biodegradable molybdenum wires (Mo, 25 μm diameter; two for the Si NM strain gauge and two for the Mg warning signal) serve as an interface for data acquisition. Inset: Optical micrograph of the water penetration sensor, which lies above the air cavity and separated from the Si NM strain gauge. The surrounding black region is the wax-based edge barrier. c) Experimental results for the sensitivity of the system to changes in pressure with and without the sensor. In both cases, the resistance changes in a linear fashion with external pressure across the range from 0–20 mmHg, with sensitivities of 16.8 ± 0.2 and 17.3 ± 0.1 Ω mmHg^{-1} for the cases with (orange) and without (blue) the sensor, respectively. The error bars represent the mean ± S.D. for three measurements. d) Resistance changes of a Si NM strain gauge (blue) and a sensor (orange) in one integrated system as a function of immersion time in PBS (pH 7.4) at 37 °C. The sensor response indicates water penetration around day 25, while the Si NM strain gauge exhibits only a slow increase in resistance on the same day.

fluctuations. The ranges of external pressure induced by manually contracting the flank might differ on different days due to the limited control on the contracting force, but the values all lie between 10 and 20 mmHg, as measured by the commercial sensor. Within this range, the change in resistance associated with contracting the rat flank defines an approximate sensitivity metric (unit: Ω mmHg^{-1}) on day x after implantation (x = 7, 14, and 21). Likewise the difference between the resistance on day x after implantation without contracting the flank and that measured on day 0 defines a change in resistance baseline ($\Delta R_{\text{day } x}$). This value divided by the sensitivity ($S_{\text{day } x}$) on the same day determines the change in pressure ($\Delta P_{\text{day } x}$) according to

$$\Delta P_{\text{day } x} = \frac{\Delta R_{\text{day } x}}{S_{\text{day } x}} \tag{3}$$

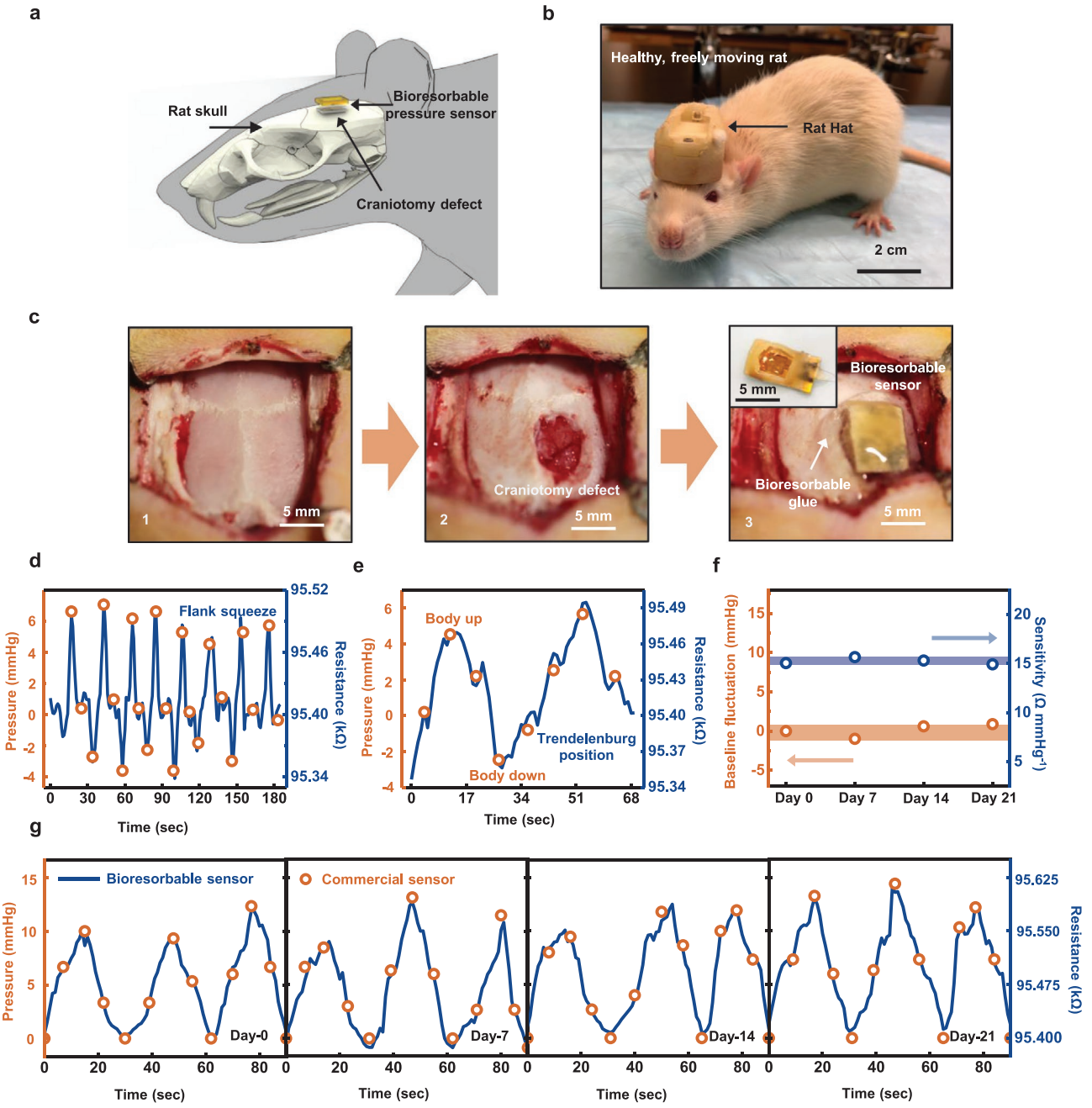

Figure 5. Long-term stable monitoring of ICP in animal models. a) Diagram of a bioresorbable device on the skull of a rat. An opening on the skull directly underneath the sensing area ensures contact of the sensor with cerebrospinal fluid (CSF). b) Integration of a measurement and protection unit that interfaces to the sensor and allows the rat to move freely within a cage environment. c) Procedures for implantation, consisting of exposing the skull area, opening a craniotomy defect, mounting the sensors above the defect and sealing the cavity with a commercial bioresorbable glue (COSEAL surgical sealant) on the edge. d,e) In vivo recordings captured using a bioresorbable sensor. Data include variations in ICP induced by compressing and releasing the flank of the animal d), by orienting the animal in the Trendelenburg (30° head-down) and reverse Trendelenburg (30° head-up) positions e) during a short period (<3 min). In all cases, the measurement results are comparable to those obtained with the commercial sensor. f) Chronic tracking of baseline (orange) and sensitivity (blue) drift through contracting and releasing the flank on day 0, 7, 14, and 21 postsurgery reveals variations of ±1.0 mmHg and ±2.1% over 3 weeks, respectively. The measurement accuracy remains largely unchanged for up to 3 weeks, without recalibration. g) Representative response curves for bioresorbable (resistance, blue line) and commercial (pressure, orange scatter) sensors on day 0, 7, 14, and 21 postsurgery.

The change between the pressure measured by the commercial sensor on day x after implantation without contracting the flank and that measured on day 0 gives the actual pressure variance ($\Delta P'_{\text{day } x}$) after x days, serving as the actual baseline pressure variance. $\Delta P_{\text{day } x}$ subtracted by $\Delta P'_{\text{day } x}$ corresponds to the baseline fluctuation of the

bioresorbable sensor on day x (unit: mmHg), which can be written as

$$\Delta P = \Delta P_{\text{day } x} - \Delta P'_{\text{day } x} = \frac{\Delta R_{\text{day } x}}{S_{\text{day } x}} - \Delta P'_{\text{day } x} \quad (4)$$

Experiments on day 7, 14, and 21 reveal fluctuations of ±1.0 mmHg in the baseline and ±2.1% of 15.0 Ω $mmHg^{-1}$ in the sensitivity over 3 weeks, respectively, consistent with standards of the AAMI. The in vivo and in vitro results show similarly stable operation. Representative response curves for bioresorbable (resistance, blue line) and commercial (pressure, orange scatter) sensors are in Figure 5g. Alternative designs for bioresorbable sensors that use t-SiO_2 for encapsulation exhibit negative drifts of ≈3 mmHg on day 25 postsurgery due primarily to partial resorption of the metal contact pads which are weakly protected by polyanhydride (≈100 µm).[15] The wax-based edge encapsulation reported here provides improved protection for the contacts, thereby eliminating this source of drift. The bioresorbable device exhibits stable response to external pressure until 28 d postsurgery, when the sensor fails to operate largely due to the biofluids penetration into the air-cavity or the breakage of the suspended film. Upon sacrificing the animals on day 28, removal of the devices reveals fractures in the Si MM and a thickness that is significantly smaller than the original value, likely due to a combination of Si dissolution and the surgical process for retrieval. The color of the wax edge encapsulation is slightly lighter than that before implantation due to water up-take. Current studies focus on systematic characterization of the degradability of natural waxes in the intracranial space. Temperature variations can also lead to changes in resistance shown in Figure S13 (Supporting Information). The effects include thermally induced 1) increases in pressure in the air-filled cavity (Figure S13b, Supporting Information; simulations), and 2) changes in the resistivity of the doped Si. Placing rats above a thermal blanket ensures constant temperature (37 °C) on the skull area to minimize these types of effects. In less well controlled conditions, addition of a temperature sensor or the use of Wheatstone bridge may be required, as described previously for bioresorbable pressure sensors with alternative designs.[15]

3. Conclusions

The bioresorbable pressure sensor systems reported here provide unique capabilities in continuous monitoring with levels of performance that meet medical guidelines for use in the intracranial space over time periods of interest for applications in recovery from traumatic brain injury and others. Stable operation followed by dissolution of the entire structure except for the wax occurs on timescales of 4 weeks; dissolution of the residual wax occurs over several months. An integrated sensor of the onset of water penetration provides an additional feature to enhance reliable interpretation of the sensor responses. The use of membranes of monocrystalline silicon as flexible encapsulation layers represents an essential design feature, as a defect-free, impermeable barrier to biofluid penetration that also bioresorbs at rates that allow for much more rapid elimination of the device compared to other approaches.[29] Optimized mechanics designs, guided by quantitative modeling, establish device geometries for which partial dissolution of this Si layer has almost no effect on the response of the sensor to changes in pressure. Tailored formulations of natural wax materials for edge encapsulation are also critically important. This type of device and the associated materials and design concepts may have further applications in additional types of sensors, wireless platforms without extruding wires, separately or in multimodal systems, such as those for measuring temperature, pH, stress/strain, motion and others of relevance to clinical medicine.

4. Experimental Section

Fabrication of Monocrystalline Silicon Micromembranes (Si MM) as Biofluid Barriers: Spin-casting at 3000 rpm for 30 s followed by baking at 110 °C for 70 s formed a layer of photoresist (AZ 5214, Microchemicals GmbH) on a silicon on insulator (SOI) wafer (top Si ≈ 1.5 µm, buried SiO_2 ≈ 1 µm, Si wafer ≈ 625 µm; SOITEC). Photolithographic exposure using a mask aligner (MA/BA6 SUSS MicroTec) at 9 mW cm^{-2} for 11 s, followed by immersion in photoresist developer (AZ 917 MIF, Microchemicals GmbH) for 25 s defined square patterns of photoresist (4 mm × 4 mm). Reactive ion etching (Samco RIE-10NR; SF_6 40 sccm, 6.7 Pa, 100 W) for 120 s removed the exposed regions of the top layer silicon. Soaking in 49% hydrofluoric acid (HF; Honeywell) for 5 min eliminated the exposed buried SiO_2. Rinsing in acetone washed the remaining photoresist away. Spin-casting at 3000 rpm for 30 s, followed by baking at 110 °C for 180 s formed another layer of photoresist (AZ 4620, Microchemicals GmbH) for photolithographic patterning (exposure with a mask aligner MA/BA6 at 9 mW cm^{-2} for 67 s, followed by development with AZ 400 K 1:2, Microchemicals GmbH, for 35 s and postbaking at 110 °C for 10 min) into square patterns (2 mm × 2 mm) as anchors at each corner of the Si/SiO_2 squares. Immersing in 49% HF for 48 h eliminated the buried SiO_2 underneath these squares. Applying droplets of acetone and drying using wipes removed the photoresist anchors. Transfer of the silicon structures to a film of PLGA (thickness: ≈16.7 µm) used a PDMS stamp (part A:part B = 4:1; Sylgard 184, Dow Corning) and the techniques of transfer printing. Formation of the PLGA film involved a process of drop-casting and slow-drying of a solution of PLGA containing ethyl acetate (5 wt%) on a hydrophobic surface prepared by immersing a Si wafer into 0.2 vol % trichloro(octadecyl) silane (Sigma) in hexane for 90 s and rinsing with DI water. The volume of PLGA solution per area during drop-casting and the concentration of PLGA in ethyl acetate determined the thickness of the resulting film.

Fabrication of Monocrystalline Boron-Doped Silicon Nanomembranes (Si NM) as Sensing Elements: Solid-state diffusion of boron (dopant BN-1250, Saint-Gobain Boron Nitride) on an SOI wafer (top Si ≈ 200 nm, buried SiO_2 ≈ 1 µm, Si wafer ≈ 625 µm; SOITEC) at 1050 °C for 20 min enhanced the piezoresistivity of the top Si. Spin-casting at 3000 rpm for 30 s followed by baking at 110 °C for 70 s formed a layer of photoresist (AZ 5214) on the SOI wafer. Photolithographic exposure using a maskless aligner (Heidelberg µPG 501), followed by developing for 9 s (AZ 917 MIF) defined a pattern of holes in an array geometry in this layer of photoresist (hole diameter: 3 µm; distance between centers of two adjacent holes: 50 µm). Reactive ion etching (Samco RIE-10NR; SF_6 40 sccm, 6.7 Pa, 100 W) for 50 s removed the exposed regions of the top layer of silicon. Soaking in 49% HF for 30 min removed the buried SiO_2. Spin-casting poly(methyl methacrylate) (PMMA; 3000 rpm for 30 s; baking at 200 °C for 300 s) and diluted polyimide (DPI, polyimide in n-methyl-2-pyrrolidone as the ratio of 2:1; 3000 rpm for 30 s; baking at 110 °C for 25 s) on a Si wafer defined a receiver for transfer of the Si NM. A PDMS stamp (part A:part B = 4:1) retrieved the Si NM (1 cm × 1 cm) from the SOI wafer for transfer onto the receiver. Wiping with a cotton pad soaked in acetone removed the photoresist on the Si NM. Full curing of the DPI occurred

in a vacuum oven at 250 °C for ≈70 min. Spin-casting at 3000 rpm for 30 s followed by baking at 110 °C for 70 s formed a layer of photoresist (AZ 5214) for photolithographic patterning (exposure with a mask aligner MA/BA6 at 9 mW cm^{-2} for 11s, followed by development with AZ 917 MIF for 25 s and reactive ion etching at 6.7 Pa, 100 W with 40 sccm of SF_6 for 50 s) into serpentine patterns to define the Si NM strain gauges. Spin-casting at 3000 rpm for 30 s followed by baking at 110 °C for 25 s, 180 °C for 180 s, and 250 °C for ≈70 min formed another fully cured layer of DPI. Spin-casting at 3000 rpm for 30 s followed by baking at 110 °C for 180 s defined a layer of photoresist (AZ 4620) for photolithographic patterning (exposure with a mask aligner MA/BA6 at 9 mW cm^{-2} for 67 s, followed by development with AZ 400K 1:2 for 35 s, postbaking at 110 °C for 180 s and reactive ion etching at 26.6 Pa, 150 W with 20 sccm of O_2 for 12 min) into mechanically stable patterns of the trilayer DPI/Si NM/DPI. Removing the PMMA with boiling acetone for 30 min released the trilayer. Manual manipulation transferred this structure to a PDMS stamp (part A:part B = 4:1). Reactive ion etching (200 mtorr, 20 sccm O_2, 150 W) for 6 min removed the exposed regions of the top layer of DPI. Transfer of the Si NM/DPI to a film of PLGA (thickness: ≈8.3 μm), followed by reactive ion etching (200 mtorr, 20 sccm O_2, 150 W) for 6 min removed the DPI. Sputtering a layer of W (thickness: 300 nm) through a polyimide (Kapton) shadow mask (thickness: ≈12.5 μm) formed contact pads.

Fabrication of Mg Meander Traces as Sensors of Water Penetration: Electron beam evaporation formed a layer of Mg (thickness: 300 nm) through a polyimide (Kapton) shadow mask (thickness: ≈12.5 μm) on a film of PLGA (thickness: ≈8.3 μm). Assembly of the Si MM/PLGA (1.5 μm/8.3 μm) and the Mg/PLGA (300 nm/8.3 μm) by lamination at a temperature above the T_g of PLGA integrated the Mg water penetration sensor into Si MM encapsulation system.

Assembly of Bioresorbable Pressure Sensor Systems: Laser cutting (LPKF Protolaser R) structured a Mg foil (≈100 μm; Goodfellow) into rectangular patterns (6 mm × 8 mm) with a trench etched into each of their surfaces (2 mm × 2.4 mm × 0.06 mm). Immersion in 2% hydrochloride acid for 10 s removed the superficial magnesium oxide. Assembly of the Si MM encapsulation layer and the Si NM strain gauge onto the Mg substrate at a temperature above the T_g of PLGA bonded the structures together. Joining Mo wires to the W pads with a conductive wax material (weight ratio, W microparticles: Candelilla wax = 16:1) enabled connection to external data acquisition electronics.

Fabrication of Natural Wax as Edge Barriers: Placing a piece of PDMS (part A:part B = 4:1) with lateral dimensions smaller than the Si MM but larger than the trench onto the top surface of a device, followed by immersing the entire structure in melted wax (CB10, CB41, CB32, and CB01) for several seconds formed a layer of wax encapsulation (thickness: ≈300 μm). For the case of PBTPA with wax, immersing the entire structure in a mixture of 115 μL of 4-pentenoic anhydride (4PA), 558 μL of 1,3,5-triallyl-1,3,5-triazine-2,4,6(1H,3H,5H)-trione (TTT), 528 μL of 1,4-butanedithiol, 3 mg of 2-hydroxy-4'-(2-hydroxyethoxy)-2-methylpropiophenone (photoinitiator) and a certain ratio of Candelilla wax (0, 5, 10, 20, and 30 wt%) at a temperature above the T_m of the Candelilla wax for several seconds, followed by UV exposure (4-watt combo UV lamp; 365 nm) for 2 min, formed a layer of PBTPA with wax (thickness: ≈300 μm). Removing the PDMS with wax on top exposed the Si MM, while leaving wax as a biofluid barrier on the edges. Another UV exposure for 10 min fully cured the PBTPA in the edge regions.

Interconnecting the Data Acquisition System: Connecting Mo wires to a digital multimeter (DMM; USB-4065; National Instruments) by hook probes enabled recording of resistance of the Si NM strain gauges and Mg traces, via a LabVIEW SignalExpress software interface on a personal computer. A 6.5-digit resolution setting ensured a low level of noise during device data acquisition.

Evaluation of Natural Wax-Based Edge Barriers: The test structures used serpentine traces of Mg (thickness: 300 nm) formed by electron beam evaporation and contact pads of W (thickness: 300 nm) by sputter deposition, both through corresponding polyimide (Kapton) shadow masks (thickness: ≈12.5 μm) on a film of PLGA (thickness: ≈8.3 μm) on a Si wafer (thickness: ≈525 μm). Another film of PLGA (thickness: ≈16.7 μm) with a Si MM (4 mm × 4 mm × 1.5 μm) on top placed above the Mg trace served as a top encapsulation. Joining Mo wires to the W pads by conductive wax enabled connection to external data acquisition electronics. Soaking the entire structures, encapsulated by different kinds of wax-based edge barriers, in PBS (pH 7.4) at 37 °C enabled daily monitoring of the resistance of the Mg traces by the DMM. For structures to evaluate interfacial water penetration, dip-coating into melted wax formed a layer of wax (1 cm × 1 cm × 300 μm) on a Si wafer (2 cm × 1 cm × 525 μm). Inspection using an optical microscope served as the basis for tracking water penetration through the wax-Si interface due to immersion in PBS (pH 7.4) at 37 °C. Three-point bending tests used the ASTM D790 standard test method on samples of wax (61 mm × 12.7 mm × 3 mm) with a tensile strength tester (Sintech 20G). A scanning electron microscope (SEM) equipped with EDAX (Hitachi SU8030) allowed measurements of the elemental composition and phase distribution of PBTPA with wax.

Evaluation of Long-Term Sensing Stability In Vitro: Placing a bioresorbable sensor and a commercial sensor (NeuLog, USA) inside the barrel of a syringe partially filled with PBS (pH 7.4) at 37 °C allowed for control of pressure across a range relevant to that in the intracranial cavity. Moving the plunger component of the syringe with a syringe pump (Harvard Apparatus) provided a means for automated and precise control of the pressure inside the syringe. Daily comparisons between the resistance response of the bioresorbable sensor and the pressure response of the commercial sensor defined the accuracy and stability.

Evaluating the Hydrolysis Kinetics of Monocrystalline Silicon Encapsulation: Spin-casting at 4000 rpm for 40 s followed by baking at 110 °C for 60 s formed a layer of negative photoresist (AZ nLOF 2035, Microchemicals GmbH) on a piece (1 cm × 1 cm) of an SOI wafer (top Si ≈ 1.5 μm, buried SiO_2 ≈ 1 μm, Si wafer ≈ 625 μm; SOITEC). Photolithographic exposure using a mask aligner (MA/BA6 SUSS MicroTec) at 9 mW cm^{-2} for 10 s, followed by immersion in photoresist developer (AZ 300 MIF, Microchemicals GmbH) for 30 s defined a square pattern of photoresist (1 mm × 1 mm). Electron beam evaporation of a bilayer of Cr/Au (thickness: 10 nm/100 nm), followed by a lift-off process in acetone formed an exposed square pattern on the top silicon (1 mm × 1 mm) Immersing the entire structure in PBS (pH 7.4) at 37 °C led to the dissolution of the exposed silicon. Imaging with a 3D laser confocal microscope (Olympus) defined changes in the height of the silicon surface compared to the edge of the deposited Cr/Au until complete dissolution.

Animals and Implantation Procedures: All animal studies followed the recommendations in the Guide for the Care and Use of Laboratory Animals of the National Institutes of Health, the suggestion from the panel of Euthanasia of the American Veterinary Medical Association and, the agreements with the Washington University in St Louis institutional guidelines. All procedures followed the approved protocols by the Institutional Animal Care and Use Committee (IACUC) of Washington University in St Louis (protocol no. 20 170 189). All procedures were performed under general anesthesia using isoflurane. Male Lewis rats weighing 250–350 g (Charles River) received subcutaneous injections of buprenorphine hydrochloride (0.05 mg kg^{-1}; Reckitt Benckiser Healthcare) for pain management and ampicillin (50 mg kg^{-1}; Sage Pharmaceuticals) to prevent infection at the implantation site before the surgical process. Device implantation involved a surgical process of anaesthetizing the rat with isoflurane gas, holding the head in a stereotaxic frame, opening a craniectomy and dura, placing a bioresorbable sensor on the cortical surface, and sealing the craniectomy with a commercial bioresorbable glue (COSEAL surgical sealant). Securing a plastic protector hat (8507 Rat Hat top and 8508 Rat Hat bottom; Pinnacle Technology Inc.) to the rat's skull by transcranial screws (#0-80, 1/8" stainless steel screws; Component Supply) and dental cement (Prime-Dent Flowable Composite A2 – 4 S) kept the wires for chronic monitoring. Three animals were used to characterize the chronic stability of bioresorbable sensors (N = 3). The surgeons provided appropriate postoperative care along with analgesia minimum of 3 d postsurgery. The surgeons weighed animals every 3 d postimplantation.

Chronic Monitoring of Intracranial Pressure in Animal Models: In vivo functional studies were performed on day 7, 14, and 21 after implantation. The animals received subcutaneous injections of buprenorphine hydrochloride (0.05 mg kg^{-1}; Reckitt Benckiser Healthcare) for pain management and ampicillin (50 mg kg^{-1}; Sage Pharmaceuticals) to prevent infection at the implantation site. Temporarily removing the top hat and connecting the Mo wires to a DMM by hook probes allowed data acquisition from bioresorbable sensors. Carefully squeezing and holding the rat's body induced increments in ICP. Embedding a clinical intracranial pressure monitor (Camino System; Model MPM-1; Integra LifeSciences) in a nearby craniectomy enabled comparison testing to demonstrate chronic accurate monitoring of bioresorbable sensors. After device characterization, the top hat was reinstalled and the rat was able to move freely within a cage environment.

Supporting Information

Supporting Information is available from the Wiley Online Library or from the author.

Acknowledgements

Q.S.Y., S.L., and Y.X. contributed equally to this work. Y.H. acknowledges the support from NSF (CMMI16335443). This work utilized Northwestern University Micro/Nano Fabrication Facility (NUFAB), which was partially supported by Soft and Hybrid Nanotechnology Experimental (SHyNE) Resource (NSF ECCS-1542205), the Materials Research Science and Engineering Center (DMR-1720139), the State of Illinois, and Northwestern University. This work was supported by the Center for Bio-Integrated Electronics at Northwestern University.

Conflict of Interest

The authors declare no conflict of interest.

Keywords

bioabsorbable electronics, biomedical implants, pressure sensors, transient electronics

Received: December 26, 2019
Revised: January 31, 2020
Published online: March 1, 2020

[1] G. Jiang, *Front. Neurosci.* **2010**, *4*, 205.
[2] L. Yu, B. Kim, E. Meng, *Sensors* **2014**, *14*, 20620.
[3] A. J. Sit, *J. Glaucoma* **2009**, *18*, 272.
[4] M. Czosnyka, *J. Neurol., Neurosurg. Psychiatry* **2004**, *75*, 813.
[5] M. M. Tisdall, M. Smith, *Br. J. Anaesth.* **2007**, *99*, 61.
[6] C. M. Boutry, H. Chandrahalim, P. Streit, M. Schinhammer, A. C. Hänzi, C. Hierold, *Philos. Trans. R. Soc., A* **2012**, *370*, 2418.
[7] M. J. Rosner, D. P. Becker, *Neurosurgery* **1976**, *23*, 494.
[8] W. C. Clark, M. S. Muhlbauer, R. Lowrey, M. Hartman, M. W. Ray, C. B. Watridge, *Neurosurgery* **1989**, *25*, 20.
[9] S.-W. Hwang, H. Tao, D.-H. Kim, H. Cheng, J.-K. Song, E. Rill, M. A. Brenckle, B. Panilaitis, S. M. Won, Y.-S. Kim, Y. M. Song, K. J. Yu, A. Ameen, R. Li, Y. Su, M. Yang, D. L. Kaplan, M. R. Zakin, M. J. Slepian, Y. Huang, F. G. Omenetto, J. A. Rogers, *Science* **2012**, *337*, 1640.
[10] W. Bai, H. Yang, Y. Ma, H. Chen, J. Shin, Y. Liu, Q. Yang, I. Kandela, Z. Liu, S.-K. Kang, C. Wei, C. R. Haney, A. Brikha, X. Ge, X. Feng, P. V. Braun, Y. Huang, W. Zhou, J. A. Rogers, *Adv. Mater.* **2018**, *30*, 1801584.
[11] L. Lu, Z. Yang, K. Meacham, C. Cvetkovic, E. A. Corbin, A. Vázquez-Guardado, M. Xue, L. Yin, J. Boroumand, G. Pakeltis, T. Sang, K. J. Yu, D. Chanda, R. Bashir, R. W. Gereau, X. Sheng, J. A. Rogers, *Adv. Energy Mater.* **2018**, *8*, 1703035.
[12] D. Lu, T. Liu, J. Chang, D. Peng, Y. Zhang, J. Shin, T. Hang, W. Bai, Q. Yang, J. A. Rogers, *Adv. Mater.* **2019**, *31*, 1902739.
[13] Q. Guo, J. Koo, Z. Xie, R. Avila, X. Yu, X. Ning, H. Zhang, X. Liang, S. B. Kim, Y. Yan, M. R. MacEwan, H. M. Lee, A. Song, Z. Di, Y. Huang, Y. Mei, J. A. Rogers, *Adv. Funct. Mater.* **2019**, *29*, 1905451.
[14] S.-K. Kang, R. K. J. Murphy, S.-W. Hwang, S. M. Lee, D. V. Harburg, N. A. Krueger, J. Shin, P. Gamble, H. Cheng, S. Yu, Z. Liu, J. G. McCall, M. Stephen, H. Ying, J. Kim, G. Park, R. C. Webb, C. H. Lee, S. Chung, D. S. Wie, A. D. Gujar, B. Vemulapalli, A. H. Kim, K.-M. Lee, J. Cheng, Y. Huang, S. H. Lee, P. V. Braun, W. Z. Ray, J. A. Rogers, *Nature* **2016**, *530*, 71.
[15] J. Shin, Y. Yan, W. Bai, Y. Xue, P. Gamble, L. Tian, I. Kandela, C. R. Haney, W. Spees, Y. Lee, M. Choi, J. Ko, H. Ryu, J.-K. Chang, M. Pezhouh, S.-K. Kang, S. M. Won, K. J. Yu, J. Zhao, Y. K. Lee, M. R. MacEwan, S.-K. Song, Y. Huang, W. Z. Ray, J. A. Rogers, *Nat. Biomed. Eng.* **2019**, *3*, 37.
[16] J. Shin, Z. Liu, W. Bai, Y. Liu, Y. Yan, Y. Xue, I. Kandela, M. Pezhouh, M. R. MacEwan, Y. Huang, W. Z. Ray, W. Zhou, J. A. Rogers, *Sci. Adv.* **2019**, *5*, aaw1899.
[17] W. Bai, J. Shin, R. Fu, I. Kandela, D. Lu, X. Ni, Y. Park, Z. Liu, T. Hang, D. Wu, Y. Liu, C. R. Haney, I. Stepien, Q. Yang, J. Zhao, K. R. Nandoliya, H. Zhang, X. Sheng, L. Yin, K. MacRenaris, A. Brikha, F. Aird, M. Pezhouh, J. Hornick, W. Zhou, J. A. Rogers, *Nat. Biomed. Eng.* **2019**, *3*, 644.
[18] J. Koo, M. R. MacEwan, S.-K. Kang, S. M. Won, M. Stephen, P. Gamble, Z. Xie, Y. Yan, Y.-Y. Chen, J. Shin, N. Birenbaum, S. Chung, S. B. Kim, J. Khalifeh, D. V. Harburg, K. Bean, M. Paskett, J. Kim, Z. S. Zohny, S. M. Lee, R. Zhang, K. Luo, B. Ji, A. Banks, H. M. Lee, Y. Huang, W. Z. Ray, J. A. Rogers, *Nat. Med.* **2018**, *24*, 1830.
[19] K. J. Yu, D. Kuzum, S.-W. Hwang, B. H. Kim, H. Juul, N. H. Kim, S. M. Won, K. Chiang, M. Trumpis, A. G. Richardson, H. Cheng, H. Fang, M. Thompson, H. Bink, D. Talos, K. J. Seo, H. N. Lee, S.-K. Kang, J.-H. Kim, J. Y. Lee, Y. Huang, F. E. Jensen, M. A. Dichter, T. H. Lucas, J. Viventi, B. Litt, J. A. Rogers, *Nat. Mater.* **2016**, *15*, 782.
[20] H. Tao, S.-W. Hwang, B. Marelli, B. An, J. E. Moreau, M. Yang, M. A. Brenckle, S. Kim, D. L. Kaplan, J. A. Rogers, F. G. Omenetto, *Proc. Natl. Acad. Sci. USA* **2014**, *111*, 17385.
[21] C. M. Boutry, L. Beker, Y. Kaizawa, C. Vassos, H. Tran, A. C. Hinckley, R. Pfattner, S. Niu, J. Li, J. Claverie, Z. Wang, J. Chang, P. M. Fox, Z. Bao, *Nat. Biomed. Eng.* **2019**, *3*, 47.
[22] G. Lee, S.-K. Kang, S. M. Won, P. Gutruf, Y. R. Jeong, J. Koo, S.-S. Lee, J. A. Rogers, J. S. Ha, *Adv. Energy Mater.* **2017**, *7*, 1700157.
[23] S. H. Kim, H. J. Lee, J.-C. Yoo, H. J. Park, J. Y. Jeong, Y. B. Seo, M. T. Sultan, S. H. Kim, O. J. Lee, C. H. Park, *J. Biomater. Sci., Polym. Ed.* **2018**, *29*, 997.
[24] S.-K. Kang, S.-W. Hwang, H. Cheng, S. Yu, B. H. Kim, J.-H. Kim, Y. Huang, J. A. Rogers, *Adv. Funct. Mater.* **2014**, *24*, 4427.
[25] S.-K. Kang, S.-W. Hwang, S. Yu, J.-H. Seo, E. A. Corbin, J. Shin, D. S. Wie, R. Bashir, Z. Ma, J. A. Rogers, *Adv. Funct. Mater.* **2015**, *25*, 1789.
[26] H. Fang, J. Zhao, K. J. Yu, E. Song, A. B. Farimani, C.-H. Chiang, X. Jin, Y. Xue, D. Xu, W. Du, K. J. Seo, Y. Zhong, Z. Yang, S. M. Won, G. Fang, S. W. Choi, S. Chaudhuri, Y. Huang, M. A. Alam, J. Viventi, N. R. Aluru, J. A. Rogers, *Proc. Natl. Acad. Sci. USA* **2016**, *113*, 11682.
[27] Y. K. Lee, K. J. Yu, Y. Kim, Y. Yoon, Z. Xie, E. Song, H. Luan, X. Feng, Y. Huang, J. A. Rogers, *ACS Appl. Mater. Interfaces* **2017**, *9*, 42633.
[28] S.-K. Kang, G. Park, K. Kim, S.-W. Hwang, H. Cheng, J. Shin, S. Chung, M. Kim, L. Yin, J. C. Lee, K.-M. Lee, J. A. Rogers, *ACS Appl. Mater. Interfaces* **2015**, *7*, 9297.

[29] Y. K. Lee, K. J. Yu, E. Song, A. Barati Farimani, F. Vitale, Z. Xie, Y. Yoon, Y. Kim, A. Richardson, H. Luan, Y. Wu, X. Xie, T. H. Lucas, K. Crawford, Y. Mei, X. Feng, Y. Huang, B. Litt, N. R. Aluru, L. Yin, J. A. Rogers, *ACS Nano* **2017**, *11*, 12562.
[30] A. Palmroth, T. Salpavaara, J. Lekkala, M. Kellomäki, *Adv. Mater. Technol.* **2019**, *4*, 1900428.
[31] L. Y. Chen, B. C.-K. Tee, A. L. Chortos, G. Schwartz, V. Tse, D. J. Lipomi, H.-S. P. Wong, M. V. McConnell, Z. Bao, *Nat. Commun.* **2014**, *5*, 5028.
[32] L. Yin, H. Cheng, S. Mao, R. Haasch, Y. Liu, X. Xie, S.-W. Hwang, H. Jain, S.-K. Kang, Y. Su, R. Li, Y. Huang, J. A. Rogers, *Adv. Funct. Mater.* **2014**, *24*, 645.
[33] S. M. Won, J. Koo, K. E. Crawford, A. D. Mickle, Y. Xue, S. Min, L. A. McIlvried, Y. Yan, S. B. Kim, S. M. Lee, B. H. Kim, H. Jang, M. R. MacEwan, Y. Huang, R. W. Gereau, J. A. Rogers, *Adv. Funct. Mater.* **2018**, *28*, 1801819.
[34] I. Bonaduce, M. P. Colombini, *J. Chromatogr. A* **2004**, *1028*, 297.
[35] U. Wolfmeier, H. Schmidt, F.-L. Heinrichs, G. Michalczyk, W. Payer, W. Dietsche, K. Boehlke, G. Hohner, J. Wildgruber, *Ullmann's Encyclopedia of Industrial Chemistry*, Wiley-VCH Verlag GmbH & Co. KGaA, Weinheim, Germany **2000**.
[36] Y. M. Pogosyan, T. V. Khanamiryan, A. Y. Pogosyan, E. K. Avetisyan, S. S. Burnazyan, *Balkan J. Stomatol.* **2011**, *15*, 142.
[37] L. Wang, Y. Gao, F. Dai, D. Kong, H. Wang, P. Sun, Z. Shi, X. Sheng, B. Xu, L. Yin, *ACS Appl. Mater. Interfaces* **2019**, *11*, 18013.
[38] L. Yin, A. B. Farimani, K. Min, N. Vishal, J. Lam, Y. K. Lee, N. R. Aluru, J. A. Rogers, *Adv. Mater.* **2015**, *27*, 1857.